JGR Space Physics

RESEARCH ARTICLE
10.1029/2019JA026987

Special Section:
Equatorial Aeronomy: New results from the 15th International Symposium on Equatorial Aeronomy (ISEA-15) and beyond

Signal Frequency Dependence of Ionospheric Scintillations: An Indicator of Irregularity Spectrum Characteristics

A. Bhattacharyya[1], P. Gurram[1], B. Kakad[1], S. Sripathi[1], and S. Sunda[2]

[1]Indian Institute of Geomagnetism, New Panvel, Navi Mumbai, India, [2]Airports Authority of India, Ahmedabad, India

Abstract Multifrequency scintillation observations show that strong amplitude scintillations on very high frequency (VHF) signals are accompanied by weak L-band scintillations near the dip equator and strong L-band scintillations in equatorial ionization anomaly (EIA) region. For several decades this has been attributed to higher ambient plasma density in the EIA region. Recent work suggests that occurrence of stronger L-band scintillations in the EIA region requires that the intermediate-scale (~100 m to few km) ionospheric irregularity spectrum in this region be significantly shallower than that in the equatorial region. However, this has not been established so far. Signal frequency dependence of amplitude scintillations is characterized by the frequency exponent that determines the dependence on signal frequency of the S_4 index: the standard deviation of normalized intensity fluctuations. In this paper, theoretical calculations of the frequency exponent for VHF and L-band signals are carried out using different irregularity spectra and compared with observations in order to characterize power-law irregularity spectra in different latitude zones. Intermediate-scale irregularities in the equatorial and low-latitude region, which are aligned with the geomagnetic field, are described by a two-dimensional model. Model simulations show that the frequency exponent derived from S_4 indices for VHF and L-band signals is determined only by the characteristics of the irregularity spectrum and hence can be utilized to identify the nature of the power-law irregularity spectrum. Frequency exponents computed using VHF and L-band observations near the dip equator and EIA regions show distinct patterns, which clearly indicate steep and shallow irregularity spectra, respectively, in these regions.

Key Points:
- Simulated scintillations show that signal frequency dependence of S_4 is determined by irregularity spectrum, not ambient plasma density
- Frequency exponent for VHF and L-band indicates steeper power-law irregularity spectrum near dip equator than at 10°N geomagnetic latitude
- Shallow irregularity spectrum found in equatorial ionization anomaly region is critical for strong L-band scintillations recorded there

Correspondence to:
A. Bhattacharyya,
archana.bhattacharyya@gmail.com

Citation:
Bhattacharyya, A., Gurram, P., Kakad, B., Sripathi, S., & Sunda, S. (2019). Signal Frequency Dependence of Ionospheric Scintillations: An Indicator of Irregularity Spectrum Characteristics. *Journal of Geophysical Research: Space Physics*, *124*. https://doi.org/10.1029/2019JA026987

Received 30 MAY 2019
Accepted 4 SEP 2019
Accepted article online 11 OCT 2019

©2019. American Geophysical Union. All Rights Reserved.

1. Introduction

Strong scintillations are often encountered on L-band signals received in the equatorial ionization anomaly (EIA) region during nighttime, due to scattering by ionospheric irregularities produced by the growth of the Rayleigh-Taylor (R-T) instability in the postsunset equatorial ionosphere. This makes the EIA region the most vulnerable to degradation of the performance of satellite-based communication and navigation systems such as the Global Navigation Satellite Systems (GNSS), particularly during solar cycle maximum conditions (Basu et al., 1988; Dasgupta et al., 2004; de Paula et al., 2010; Kintner et al., 2001; Moraes et al., 2011). After initiation of the R-T instability on the bottom side of the postsunset equatorial F layer, a density-depleted region referred to as the equatorial plasma bubble (EPB) rises to the linearly stable topside of the equatorial F layer and develops structure. As this is an interchange instability involving the interchange of entire flux tubes, irregularities formed at different altitudes over the dip equator are mapped to off-equatorial ionosphere along geomagnetic field lines (Huba & Joyce, 2010; Retterer, 2010a; Yokoyama, 2017; Yokoyama et al., 2014). For a radio signal propagating through a thick layer of ionospheric irregularities to a ground receiver, maximum contribution to scintillations comes from the irregularities in the ionospheric F peak region, where the ambient density is maximum. Therefore, the strength of amplitude scintillations recorded at different latitudes depends on the characteristics of the irregularities of appropriate scale lengths, encountered at the ionospheric penetration points (IPPs) of the signal paths in the vicinity of the corresponding F layer peaks. Irregularities with scale sizes close to the Fresnel scale ($=\sqrt{2\lambda H}$, where λ is the signal wavelength and H is the average distance of the irregularity layer from the receiver along the signal path) contribute the most to amplitude scintillations. The S_4 index, which is the standard deviation of normalized intensity fluctuations, is used as a measure of the strength of amplitude scintillations.

It is well known that while L-band scintillations are strongest near the peak of the EIA region, they are much weaker near the dip equator (Bhattacharyya et al., 2003; de Oliveira Moraes et al., 2018; Groves et al., 1997;

Muella et al., 2009; Mullen et al., 1985; Nishioka et al., 2011; Sripathi et al., 2008; Whalen, 2009). In the past this has been attributed entirely to the higher ambient plasma density in the EIA region (Whalen, 2009). However, using very high frequency (VHF) and L-band scintillation observations by a network of stations, and modeling the scintillations, Bhattacharyya et al. (2017) concluded that irregularities encountered by the signals near *F* peak in the EIA region must have a significantly shallower spectrum than the irregularities present near equatorial *F* peak. They also showed that enhanced ambient plasma density would not be able to produce strong L-band scintillations if the irregularity power-law spectrum had a steep slope. Considering H to be 350 km, Fresnel scales for 251-MHz and 1.575-GHz signals are 914 and 365 m, respectively. Therefore, only the spectrum of intermediate scale length (~100 m to few km) irregularities is of interest here. At present, 3-D simulations of development of EPBs either do not have the spatial resolution to yield the irregularity spectrum in intermediate-scale range or are not coupled to realistically evolving background ionosphere (Huba & Joyce, 2010; Keskinan et al., 2003; Retterer, 2010a, Yokoyama et al., 2014, Yokoyama, 2017). Power spectral analysis of scintillation data is useful for directly estimating the spectral characteristics of irregularities only under weak scintillation conditions (Yeh & Liu, 1982). Hence, it is necessary to calculate some parameter from scintillation data, which would provide a definitive picture of the irregularity spectrum at the dip equator and in EIA region, under all scattering conditions. In this paper, on the basis of theoretical calculations, the frequency exponent described in the next section is identified as such a parameter. This parameter is then estimated from amplitude scintillations on signals of frequencies 251 MHz and 1.575 GHz, recorded near the dip equator and in the EIA region, for comparison with the theoretical results. Frequency exponents computed from observations of amplitude scintillations on signals of frequencies 251 MHz and 1.575 GHz, in the dip equatorial and EIA regions, show unequivocally the distinct nature of the irregularity spectra for the two locations.

2. Theoretical Results for the Frequency Exponent

A two-dimensional model is frequently used to describe intermediate scale length irregularities in the equatorial ionosphere, as they are aligned with the geomagnetic field. S_4 index for weak scintillations on a signal of frequency f, produced by isotropic three-dimensional irregularities characterized by a single-component power-law spectrum with slope $-p$, with an outer scale much greater than the Fresnel scale, has a signal frequency dependence of the form $S_4 \propto f^{-n}$, where $n = (p+2)/4$ (Yeh & Liu, 1982). The corresponding relationship for isotropic two-dimensional irregularities is derived here under the phase screen approximation. In this approximation, the irregularity layer is substituted by a phase-changing screen. The incident radio wave of wavelength λ, propagating in the z direction, is assumed to have the form $A_0 \exp[i(kz - \omega t)]$ where $k = 2\pi/\lambda$ and A_0 is its amplitude before it enters the irregularity layer. For the 2-D irregularities considered in the paper, the phase perturbation ϕ imposed by the screen located at $z = 0$ is a function of only the coordinate x, transverse to the geomagnetic field, which is assumed to be in the y direction:

$$\phi(x) = -\lambda r_e \Delta N_T(x); \Delta N_T(x) = \int \Delta N(x,z)\, dz. \tag{1}$$

Here, ΔN is the fluctuation in electron density, and r_e is the classical electron radius. Autocorrelation function for $\phi(x)$ is given by

$$B_\phi(x) = (\lambda r_e)^2 2\pi L \int_{-\infty}^{\infty} \Phi_{\Delta N}(k_x, 0)\, e^{ik_x x} dk_x, \tag{2}$$

with L as the thickness of the irregularity layer and $\Phi_{\Delta N}(k_x, k_z)$ as the irregularity spectrum. Following Yeh and Liu (1982), the complex amplitude of the signal at the ground receiver located at (x,y,z) is given by

$$u(x,y,z) = \frac{ikA_0}{2\pi z} \int_{-\infty}^{\infty} e^{-i\left[\phi(x') + \frac{k}{2z}(x-x')^2\right]} dx' \int_{-\infty}^{\infty} e^{-i\frac{k}{2z}(y-y')^2} dy'. \tag{3}$$

u does not depend on y, so y shall be dropped in the future. Writing $u(x,z)$ as follows:

$$u(x,z) = A_0 \exp[\chi(x,z) - iS_1(x,z)], \tag{4}$$

and under the assumption of weak scintillations produced by a shallow screen so that quadratic and higher order terms in χ and ϕ may be neglected in the expansion of exponentials in equations (3) and (4), it is seen that log-amplitude χ has the form

$$\chi(x,z) = \frac{1}{2}\sqrt{\frac{k}{\pi z}}\int_{-\infty}^{\infty}\phi(x')\left\{\sin\left[\frac{k}{2z}(x-x')^2\right] - \cos\left[\frac{k}{2z}(x-x')^2\right]\right\}dx'. \quad (5)$$

Autocorrelation function for χ is now given by

$$B_\chi(x) = 2\pi L\lambda^2 r_e^2\int_{-\infty}^{\infty}\Phi_{\Delta N}(k_x,0)\sin^2\left(\frac{z}{2k}k_x^2\right)e^{ik_x x}\,dk_x. \quad (6)$$

For weak scintillations,

$$S_4^2 = 4\chi^2 = 8\,\pi L\lambda^2 r_e^2\int_{-\infty}^{\infty}\Phi_{\Delta N}(k_x,0)\sin^2\left(\frac{z}{2k}k_x^2\right)dk_x. \quad (7)$$

The sine-squared term in the integral is the Fresnel filter function, which ensures that the contribution to weak amplitude scintillations from irregularities much larger than the Fresnel scale $\left(=\sqrt{2\lambda z}\right)$ is negligible. Thus, if the two-dimensional irregularity spectrum is of the single-component power-law form with outer scale much greater than the Fresnel scale, $\Phi_{\Delta N}(k_x,0)\propto k_x^{-m}$ in the integrand in equation (7). Then, it follows from equation (7) that the signal frequency dependence of S_4 is of the form $S_4 \propto f^{-n}$ with $n = (m+3)/4$.

For a two-component power-law spectrum, there is no analytical result for the frequency exponent n, even under the assumption of weak scintillations on both the signals. When scintillation on both frequencies is weak, S_4 indices for two signals with frequencies $f_1 = 1541.5$ MHz and $f_2 = 3945.5$ MHz have been numerically estimated for a two-component power-law spectrum of the form (Franke et al., 1984)

$$\Phi_{\Delta N}(q) = C_{\Delta N}\left(q_0^2+q^2\right)^{-m_1/2}\left(q_b^2+q^2\right)^{(m_1-m_2/2)}. \quad (8)$$

Here, $q_0 = 2\pi/R_0$, and $q_b = 2\pi/R_b$, with R_0 and R_b being the outer and break scale lengths, respectively, and the dependence of the constant $C_{\Delta N}$ on q_0 and q_b is determined by the values of m_1 and m_2. Dependence of n on the break scale length R_b studied by these authors using their numerical results shows that when R_b is much greater than the Fresnel scale at both frequencies, n tends to $(m_2+3)/4$ and when R_b is much smaller than the Fresnel scale at both frequencies, n tends to $(m_1+3)/4$. The frequency exponent n is calculated using S_4 indices for two different signal frequencies. On the lower frequency signal, a major part of the observed scintillations may not fall in the weak category, and therefore, n may deviate from the "weak scintillation" value. For scintillations that are not weak, it is necessary to use strong scatter theory to compute n. In the past, variation of n estimated from S_4 indices for L-band and C-band signals recorded at Ascension Island, near the crest of the EIA region, was explained using a phase screen model for the irregularities (Franke & Liu, 1983, 1985). Theoretical results reported in these papers were obtained by computation of the wavefield on the ground, after the signal propagated through a one-dimensional phase screen characterized by phase variations produced by the irregularities. In the present paper, a 2-D model of the irregularities is used to estimate n from the S_4 indices for 251-MHz and 1.575-GHz signals computed under all scattering conditions, by solving the equation satisfied by the fourth moment of the complex amplitude of the wave (Bhattacharyya et al., 2017).

For the calculation of the S_4 index under all scattering conditions, instead of a phase screen, finite thickness of the irregularity layer is taken into consideration. Once it enters the irregularity layer, the wave acquires a complex amplitude on account of the phase variations imposed by the irregularities, which depend on the transverse coordinate x. As the wave traverses through the irregularity layer, amplitude scintillations also build up, and the complex amplitude is a function of x and z. The fourth moment of the complex amplitude u (x,z) of the wave is defined as follows:

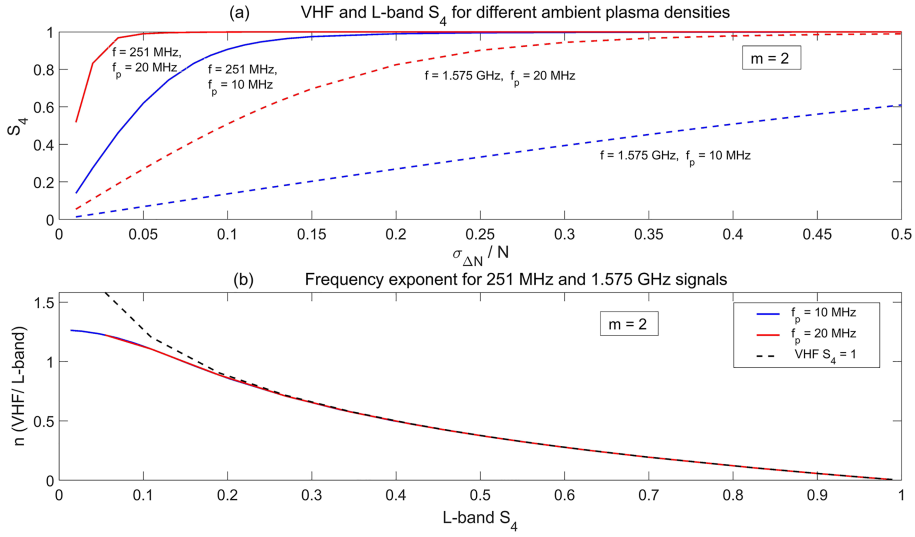

Figure 1. (a) Variation of S_4 indices for simulated scintillations on 251 MHz (very high frequency [VHF]) and 1.575 GHz (L-band) signals, with the normalized density fluctuation strength $\sigma_{\Delta N}/N$. Results are shown for two ambient plasma frequencies: $f_P = 10$ MHz and $f_P = 20$ MHz and a single-component irregularity spectrum with a slope of -2 ($m = 2$). (b) Frequency exponent n computed from the VHF and L-band S_4 indices shown in (a) as a function of L-band S_4. Black dashed curve is a plot of n versus L-band S_4 when VHF $S_4 = 1$.

$$\Gamma_4(x_1, x_2, x_3, x_4, z) = u(x_1, z)\, u(x_2, z)\, u^*(x_3, z)\, u^*(x_4, z), \tag{9}$$

where x axis is taken to be in the magnetic east-west direction. The equation satisfied by Γ_4 in the course of the signal propagating through a thick irregularity layer followed by free space to the ground receiver (Yeh & Liu, 1982) is solved using the split-step method (Bhattacharyya & Yeh, 1988). The irregularities are characterized by either a single-component power-law spectrum with slope $-m$ as given in equation (4) of Bhattacharyya et al. (2017) or a two-component power-law spectrum of the form given in equation (8). For the particular case of $m_1 = 2$ and $m_2 = 4$, which is considered in this paper, the constant $C_{\Delta N} = \sigma_{\Delta N}^2 \left(q_b^2 - q_0^2\right)/2\pi \ln\left(q_b/q_0\right)$. Here, $\sigma_{\Delta N}$ is the standard deviation of electron density fluctuations. It can be seen from equation (9) that the S_4 index is a special case of Γ_4 (Bhattacharyya et al., 2017). In the calculation of S_4, ambient plasma density N is assumed to be constant throughout the irregularity layer, which is effectively a region around the F layer peak, where N is a maximum. In Figure 1, results are shown for a single-component power-law irregularity spectrum with slope -2. In Figure 1a, computed S_4 indices for the two signal frequencies are shown as a function of the normalized density fluctuation strength $\sigma_{\Delta N}/N$, although S_4 depends on only $\sigma_{\Delta N}$. N is represented by the ambient plasma frequency $f_P = (Ne^2/\pi m_e)^{1/2}$, where e and m_e are the charge and mass of an electron. The reason ambient plasma density has been introduced in Figure 1a, where the x axis shows the fractional density fluctuation, is because traditionally, it has been argued that for a given percentage density fluctuation associated with the irregularities that map down from the equatorial region to the EIA region, stronger L-band scintillations are observed in the EIA region only because the ambient density is higher. This is only partially correct (Bhattacharyya et al., 2017). Two different ambient plasma frequencies are considered so that for a given percentage density fluctuation, the case with higher N represents larger density fluctuations. For a given ambient plasma frequency, S_4 index on 251 MHz increases much more rapidly with increasing irregularity strength than the S_4 index on 1.575 GHz and tends to approach a value of 1. This happens at a lower value of $\sigma_{\Delta N}/N$ for a higher background plasma density. Also, as expected, for a given $\sigma_{\Delta N}/N$, S_4 for L-band signal is significantly higher when N is higher. This is the reason why the presence of strong L-band scintillations in the EIA region, when only weak L-band scintillations are observed near the dip equator, has been attributed to the higher ambient plasma density in the EIA region. However, these results are for $m = 2$. Bhattacharyya et al. (2017) have shown that for a steep irregularity spectrum with $m = 5$, L-band scintillations tend to be weak and an increase in background plasma density is not as effective in increasing L-band S_4 as in the case of $m = 2$.

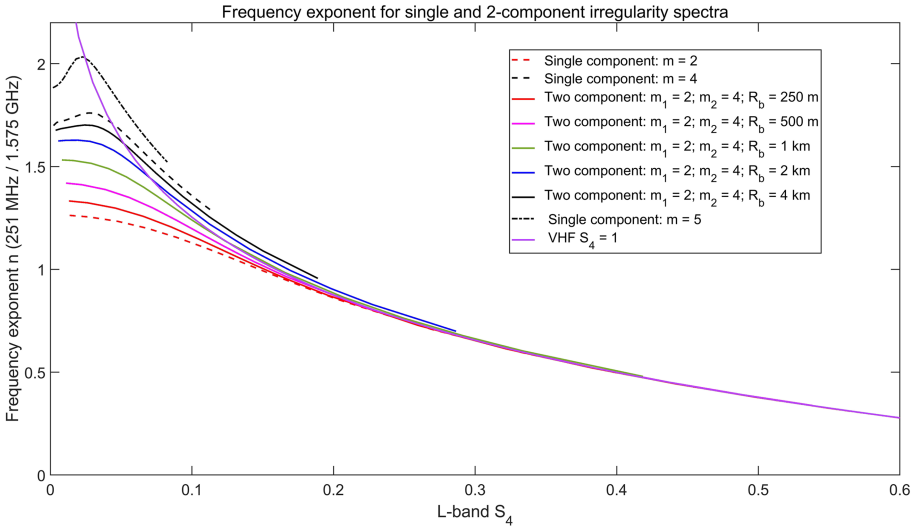

Figure 2. Frequency exponent n computed from simulated very high frequency and L-band S_4 indices as a function of L-band S_4. Irregularity spectra used in the simulations are single component with $m = 2$, 4, and 5, two-component with $m_1 = 2$, $m_2 = 4$, and break scale length $R_b = 250$ m, 500 m, 1 km, 2 km, and 4 km. The curve for very high frequency $S_4 = 1$ is also shown.

As mentioned earlier, so far, it has not been possible to unequivocally attribute the difference in L-band scintillations observed near the dip equator and in the anomaly region to the difference in the spectrum of ionospheric irregularities encountered in those regions. As can be seen from the above results, a higher ambient plasma density increases the S_4 indices for both signals. S_4 indices on both the signals also depend on other factors such as the outer scale length and thickness of the irregularity layer encountered by the signals. In Figure 1b, the frequency exponent n computed from the S_4 indices shown in Figure 1a:

$$n(f_1/f_2) = -\frac{\log[S_4(f_1)/S_4(f_2)]}{\log(f_1/f_2)}, \tag{10}$$

with $f_1 = 251$ MHz and $f_2 = 1.575$ GHz is shown as a function of the L-band S_4 index, for the two ambient plasma frequencies considered in Figure 1a. As expected, there is no difference between the curves for the two ambient plasma densities, although S_4 indices for both signals differ significantly in the two cases. In the situation where VHF S_4 approaches unity, one expects a universal curve of $A \log x$ versus x (=L-band S_4), where the constant $A = 1/\log(251/1575)$. This universal curve is shown by the black dashed line in Figure 1b. Even for L-band $S_4 < 0.2$, where VHF S_4 shows very distinct variation with $\sigma_{\Delta N}/N$ for the two ambient plasma frequencies in Figure 1a, the variation of n with L-band S_4 is the same in the two cases. This is so because the ratio of the two S_4 indices depends only on $\sigma_{\Delta N}$ for a given form of the irregularity spectrum and the L-band S_4 index is a proxy for $\sigma_{\Delta N}$ although the relationship between the two ceases to be a linear one for strong scintillations as can be seen from Figure 1a. As mentioned earlier, S_4 indices on both the signals also depend on other factors such as the outer scale length and thickness of the irregularity layer encountered by the signals. Therefore, other cases were also studied where these factors were varied. In one such case, ambient plasma frequency was kept constant in the theoretical model, while the outer scale R_0 was doubled from 10 to 20 km, keeping other factors the same. Again, no difference was seen in the plots of n versus L-band S_4, which is not shown here. Likewise, no change in n was found on doubling the thickness of the irregularity layer from 50 to 100 km, also not shown here.

For the display in Figure 2, ambient plasma frequency, R_0, and thickness of the irregularity layer were kept fixed at 10 MHz, 10 km, and 50 km, respectively, but different irregularity spectra were considered. Results are shown for single-component power-law spectra with slopes of −2, −4, and −5. Also, shown are the plots of n versus L-band S_4 for two-component power-law spectra with $m_1 = 2$ and $m_2 = 4$ but different break scale lengths. Plots are shown for R_b equal to 250 m, 500 m, 1 km, 2 km, and 4 km. It can be seen from Figure 1a that even when L-band S_4 is 0.05, scintillations on the VHF signal are no longer weak and therefore, n

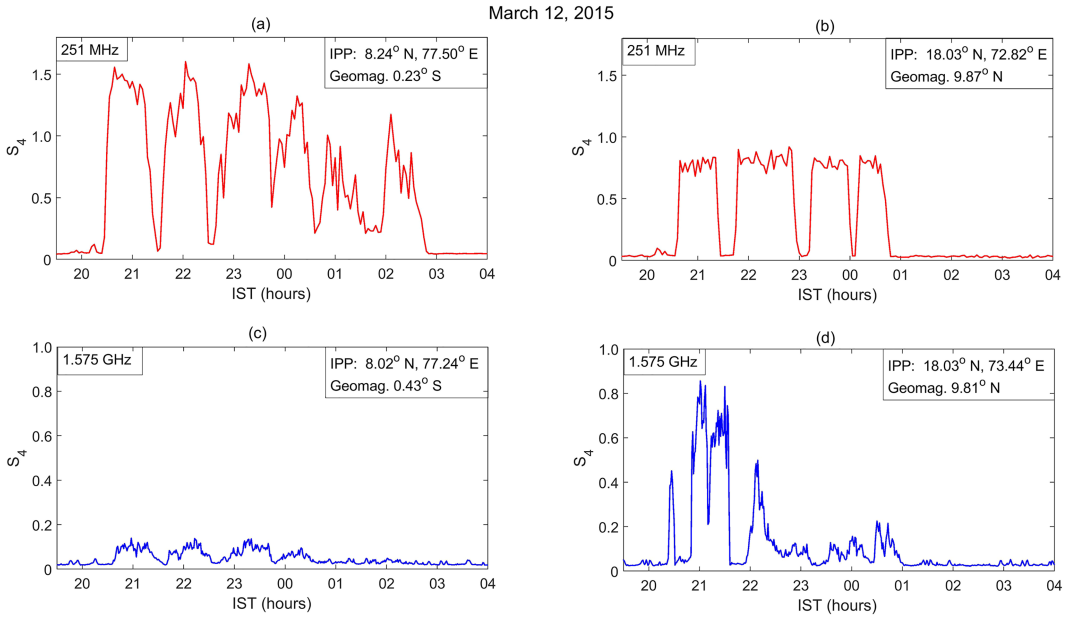

Figure 3. (a–d) S_4 indices estimated from scintillations on 251-MHz and 1.575-GHz signals recorded in dip equatorial and equatorial ionization anomaly regions, as a function of Indian Standard Time on 12 March 2015. Coordinates of the respective ionospheric penetration points are given in the figures.

deviates from the weak scintillation value. Figure 2 demonstrates that n is sensitive to the nature of the irregularity spectrum. In fact, S_4 for the VHF signal can exceed 1 when the irregularity spectrum is sufficiently steep ($m \geq 3$; Rino, 1979). This happens due to focusing of the signal by larger scale irregularities in the absence of small-scale structures, which are more effective in scattering the radio waves and thus destroying the focusing effects of the large-scale irregularities. With further increase in strength of the irregularities, even for an irregularity spectrum with a steep slope, small-scale irregularities are sufficiently strong to scatter the incident radio signal and decrease the focusing effect. At this stage VHF S_4 starts to decrease from its peak value. As a result of focusing of the VHF signal, n shows a peak for $m = 4$ and $m = 5$ and for the two-component spectrum with a break scale of 4 km. For the two-component spectrum, as R_b decreases, n shifts toward the value obtained for a single-component spectrum with the shallower slope $m_1 = 2$. This is expected from the variation of S_4 with R_b (Carrano & Rino, 2016). These results show that n is a parameter that can be computed from observations to establish the nature of the irregularity spectra encountered by VHF and L-band signals recorded at different locations.

3. Frequency Exponent From Observations

VHF and L-band scintillations recorded near the dip equator and in EIA region in the Indian sector have been used to compute n in this paper. Amplitude scintillations on a 251-MHz signal transmitted from a geostationary satellite UFO10 located at 72.4°E have been recorded at equatorial station, Tirunelveli (TIR), and off-equatorial station Mumbai (MUM). Scintillations on an L1 (1.575 GHz) signal transmitted from the geostationary satellite GSAT-10 located at 83°E were recorded at MUM and at the equatorial station Trivandrum (TRV) located close to TIR. VHF S_4 calculated for every 3-min interval of scintillations recorded at TIR and MUM on 12 March 2015 is shown as a function of Indian Standard Time in Figures 3a and 3b. S_4 for the L1 signals calculated for 1-min intervals of scintillations recorded on the L1 signal received at TRV and MUM on 12 March 2015 is plotted in Figures 3c and 3d. For computation of n, ideally, both the signals should be transmitted from the same satellite and recorded at the same station. In the present case, elevation angles for the signal paths for the VHF and L1 signals received at TIR and TRV are 78° and 77.8°, respectively, while coordinates of the IPPs at an altitude of 300 km for these signals are VHF: 8.24°N, 77.5°E (geomagnetic latitude 0.23°S), and L1: 8.02°N, 77.24°E (geomagnetic latitude 0.43°S). Hence, both the VHF and L1 signals are traversing nearly the same region of irregularities at about the same elevation angle. As seen from Figures 3a

and 3c, although the magnitudes of S_4 are very different for VHF and L-band, similarity of the patterns of temporal variation of S_4 on VHF and L1 signals indicates that the two signals are propagating through the same volume of irregularities. A similar situation exists for the VHF and L1 signals received at MUM. Signal path elevation angles are 67.6° and 65° for the VHF and L1 signals, respectively, and coordinates of the IPPs at an altitude of 300 km for these signals are VHF: 18.03°N, 72.82°E (geomagnetic latitude 9.87°N), and L1: 18.03°N, 73.44°E (geomagnetic latitude 9.81°N). In this case the two patterns differ to some extent because during the decay phase of irregularities, L-band scintillations die out faster than VHF scintillations as the shorter scale length irregularities decay earlier due to diffusion. Comparison of Figures 3a and 3c shows that this also happens at the equatorial location.

The S_4 patterns seen in Figures 3a–3d are fairly typical of scintillations recorded at these locations during vernal equinox, generally showing strong VHF scintillations near the equator with $S_4 > 1$ sometimes, while L-band scintillations are always weak ($S_4 < 0.2$). In the EIA region at about 10° geomagnetic latitude, VHF scintillations may be fairly strong but with $S_4 \leq 1$, while L-band scintillations are much stronger here than near the dip equator. Such observations were discussed by Bhattacharyya et al. (2017) for the first time in the context of the irregularity spectrum. As noted earlier, during the decay phase of irregularities, L-band scintillations die out faster than VHF scintillations due to earlier decay of shorter scale length irregularities. Therefore, the irregularity spectrum is expected to become steeper postmidnight even in the EIA region, which should also be reflected in the behavior of n. In Figures 3b and 3d, a small time shift is seen between the patterns of VHF and L-band S_4. This may be attributed to the L1 IPP being located 0.62°E of the IPP for VHF signal, considering that the irregularities generally drift eastward through the night. For the equatorial stations, the L1 IPP is only 0.26°E of the IPP for VHF signal, and therefore, the time shift is not clearly seen. For the computation of n, difference in longitudes of the VHF and L1 IPPs is taken into account by introducing time lags of about 6 and 12 min between the VHF and L1 S_4, for the equatorial and EIA regions, respectively, based on an assumed eastward drift of the irregularities of about 100 ms^{-1}. The frequency exponent n is computed at 3-min intervals. Also, in order to avoid noise in the data, n is computed when VHF $S_4 \geq 0.15$ and L1 $S_4 \geq 0.05$.

4. Frequency Exponent in Equatorial and EIA Regions

Frequency exponents computed from VHF and L1 S_4 in the equatorial region (average geomagnetic latitude = 0.33°S) and EIA region (average geomagnetic latitude = 9.84°N) for 11 days in March 2015 are plotted as a function of the respective L1 S_4 in Figure 4. Theoretical curves of n as a function of L1 S_4, shown in Figure 2, are also included in Figure 4. In addition to these, plots of n versus L-band S_4 for three fixed values of VHF S_4 (VHF S_4 = 0.7, 0.8, and 0.9) are also displayed in Figure 4. Here, the new result is the clear distinction between frequency exponents obtained from observations in the equatorial and EIA regions. In the equatorial region, high elevation angle signal paths basically encounter irregularities near the dip equator, which is the case here. It is found that the L-band S_4 generally does not exceed 0.2 and n tends to follow the steep irregularity spectrum curves. Most of the values of n obtained from equatorial observations indicate a single-component irregularity spectrum of slope between −4 and −5, resulting in some VHF $S_4 > 1$. In the EIA region, irregularity spectrum tends to be shallow ($m \leq 2$) before midnight. During this period, there are many points for the EIA region in Figure 4, which correspond to strong VHF scintillations with S_4 values between 0.7 and 0.9, produced by irregularities that also give rise to significant L-band scintillations with S_4 values between 0.2 and 0.9, but the VHF S_4 does not exceed 1. As noted in section 3, during postmidnight decay phase of irregularities, in the EIA region, also, strong VHF scintillations are accompanied by weak L-band scintillations. Steepening of the irregularity spectrum during this phase is seen in the behavior of n for L-band $S_4 < 0.1$ in the EIA region.

Figure 2 shows that for $m = 2$, the curve for n merges with the universal curve for VHF $S_4 = 1$ for L-band $S_4 > 0.2$. On the other hand, the frequency exponent curve for $m = 5$ shown in Figure 2 appears to asymptotically approach a universal curve associated with VHF $S_4 > 1$, when $\sigma_{\Delta N}/N = 90\%$. It is expected that for a spectrum with $m < 2$, the frequency exponent curve would lie below the curve for $m = 2$, because in this case, L-band S_4 is expected to be closer to VHF S_4 yielding lower values of n. According to Figure 4, many of the n values in the EIA region tend to lie between the universal curves for VHF S_4 = 0.7 and 0.9, for L-band S_4 above 0.2, indicating irregularity spectra with $m < 2$. However, it is not possible to determine whether the

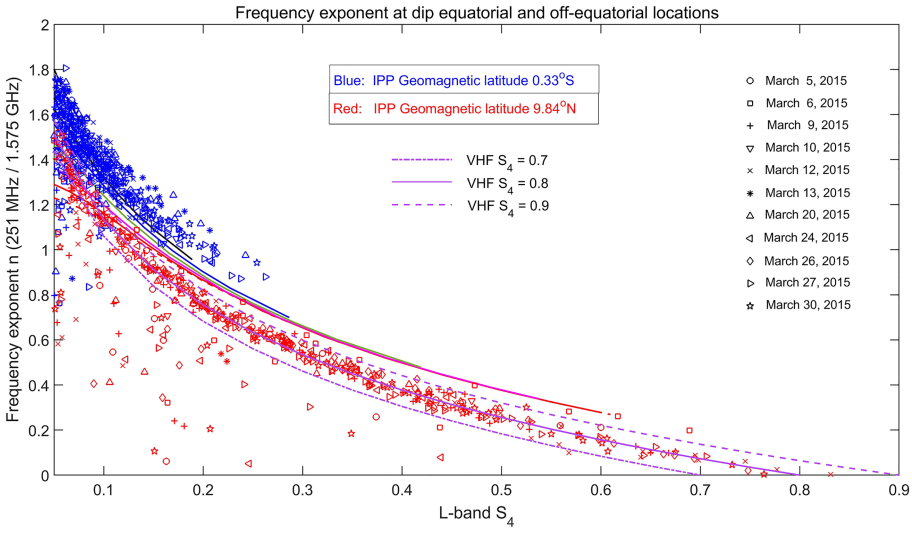

Figure 4. Frequency exponent n computed from very high frequency and L-band S_4 indices derived from scintillations on 251-MHz and 1.575-GHz signals recorded in the equatorial (blue markers) and equatorial ionization anomaly (red markers) regions, as a function of L-band S_4, for 11 days in March 2015. These are superposed on the theoretical curves of Figure 2. Curves of n for VHF $S_4 = 0.7$, 0.8, and 0.9, as a function of L-band S_4 are also shown for comparison with n derived from observations.

irregularities should be described by a single-component or a two-component spectrum and the corresponding break scale in the latter case. More accurate modeling of the observations would require a 3-D model of anisotropic irregularities with noninteger spectral indices for the irregularity spectrum, which would be undertaken in the future.

In Figure 4, there are a number of points below the curve for VHF $S_4 = 0.7$, which need an explanation. It has been mentioned in the previous section that there is a small time shift between the patterns of VHF and L-band S_4 at station Mumbai in the EIA region. This has been attributed to the L1 IPP being located 0.62°E of the IPP for VHF signal and the irregularities drifting eastward. For the equatorial stations, the L1 IPP is only 0.26°E of the IPP for VHF signal, and therefore, the time shift is not clearly seen. In the computation of n, difference in longitudes of the VHF and L1 IPPs has been taken into account by introducing time lags of about 6 and 12 min between the VHF and L1 S_4, for the equatorial and EIA regions, respectively, based on an assumed eastward drift of the irregularities of about 100 ms^{-1}. The scattered red markers below the VHF $S_4 = 0.7$ curve in Figure 4 arise due to the fact that irregularities do not always drift eastward with a speed of 100 ms^{-1}, so that the VHF and L-band radio signals recorded at Mumbai with a delay of 12 min between the two do not always propagate through the same volume of irregularities. For instance, in Figure 4 for L-band $S_4 = 0.1$, values of n below the VHF $S_4 = 0.7$ curve vary between about 0.4 and 1. The corresponding VHF S_4 values vary between 0.21 and 0.63. This is due to the mismatch between irregularities considered to be in the paths of the VHF and L-band signals.

5. Discussion and Conclusions

Forecasting of low-latitude scintillations (Carter et al., 2014), which often have detrimental effects on the performance of satellite-based navigation systems, requires knowledge of the development of intermediate-scale irregularities and their characteristics in different regions of the ionosphere. Keskinen et al. (2003) reported that ionospheric structures with extremely sharp density gradients are seen in the EIA region but not in the equatorial region in their simulation of the nonlinear development of 3-D EPBs. However, the irregularity spectrum and its relationship with scintillations were not investigated in this work. In the 3-D simulations of the development of EPBs carried out by Retterer (2010a, 2010b), spatial resolution (10 km) is inadequate for simulating the generation of irregularities that produce scintillations on VHF and L-band radio signals. However, an important result that emerged from this work was that in premidnight hours, power spectrum of spatial variations in the magnetic east-

west direction of the vertical total electron content down to a scale size of 20 km is significantly shallower in the EIA region as compared to the equatorial region. On the basis of VHF and L-band amplitude scintillation observations, it was suggested by Bhattacharyya et al. (2014, 2017) that in the course of nonlinear evolution of EPBs, the low-density topside of the equatorial F region developed more structure than the equatorial F region peak. The topside irregularities were mapped along the geomagnetic field lines to the F layer peak in the EIA region resulting in a shallower intermediate-scale irregularity spectrum there compared to the equatorial F peak region. This combined with the higher background plasma density in the EIA region gave rise to the much stronger L-band amplitude scintillations recorded there than in the equatorial region. However, the nature of the irregularity spectrum was not established because the irregularity spectrum and the ambient plasma density both contribute to the observed scintillations. In recent years, a high-resolution bubble model has been developed (Yokoyama, 2017; Yokoyama et al., 2014), where a zonal resolution of 333.6 m has been achieved. This model also shows that as an EPB grows nonlinearly in the topside of the equatorial F region, it becomes more structured than the equatorial F peak region. Spectra of the intermediate-scale irregularities associated with EPBs have also been studied using the simulation results of high-resolution bubble in a recent paper (Rino et al., 2018). In this paper, stochastic structure in evolving EPBs was obtained from the model simulations, in three-slice planes perpendicular to the geomagnetic field: one at the dip equator and two others offset at different geomagnetic latitudes. An important result from this paper is that it demonstrates that the structures from the topside of the equatorial F region above 500 km are indeed mapped along geomagnetic field lines to the F region peak (around 350 km) in the offset two-slice plane. Their results also show that the developed structures are characterized by a two-component power-law spectrum.

In situ measurements of ion density in a structured equatorial ionosphere were carried out by instruments on board the ROCSAT 1 satellite, which had a circular orbit at an altitude of 600 km, with an inclination of 35° (Su et al., 2001). These authors found that for irregularities of scale sizes in the range 200–700 m within EPBs encountered in the equatorial region at about 20 LT, the spectral index indicated a shallow slope between −0.5 and −2. This would correspond to $1.5 < m < 3$ for a 2-D irregularity spectrum considered in this paper. Spectral slopes of irregularities with scale sizes in the range 100 m to 10 km have also been estimated from in situ high-resolution measurements of ion density made by the low-inclination C/NOFS satellite in October 2008 (Rodrigues et al., 2009). The slopes were found to be $\approx -5/3$ around local midnight at the rather low altitude of ~450 km in the equatorial region, where irregularities are not expected to be in an inertial regime. This was attributed by the authors to the unusually low neutral densities during the extended solar minimum conditions that prevailed at the time, which resulted in much lower than usual ion-neutral collision frequencies at this altitude. Thus, these measurements also indicate that intermediate-scale irregularities associated with EPBs in the topside equatorial ionosphere, where ion inertia becomes important, have a shallow spectrum. In both of these works, a transition to a steeper spectrum is found at a break scale length of around 100 m. Analysis of 4 years of high-resolution C/NOFS satellite data (Rino et al., 2016) has revealed that for intermediate-scale irregularities, two-component spectra are found in the early development phase, whereas in the decay phase these irregularities tend to have a single-component spectrum. For the two component spectra studied in this paper, the shallow slopes tended to vary in the range −0.5 to −1.5, which would imply $1.5 < m < 2.5$ for the 2-D irregularity spectrum investigated in this paper. The break scale showed a tendency to be shorter at higher altitudes and could be as short as a few hundred meters. However, there is no information in this paper about the geomagnetic latitudes of the locations where measurements were made or the apex altitude over the dip equator to which these measurements could be mapped.

The present paper gives the first results based on nighttime amplitude scintillation observations and modeling that show the distinct nature of intermediate-scale irregularity spectra in the equatorial and EIA regions. Irregularities present near the peak of the postsunset equatorial ionospheric F region may give rise to very strong VHF scintillations, with $S_4 > 1$ sometimes, but only weak L-band scintillations. This is explained by a power-law irregularity spectrum, which is steep ($m \geq 4$). On the other hand, irregularities encountered by VHF and L-band signals near the F peak in EIA region may give rise to strong VHF scintillations but with S_4 always <1 accompanied by much stronger L-band scintillations than that found in the equatorial region. The frequency exponent computed from VHF and L-band scintillations recorded in these two regions

unequivocally shows that, before midnight, the intermediate-scale irregularity spectrum in the EIA region is much shallower ($m \leq 2$) than that in the equatorial region. An irregularity spectrum with a slope as steep as the equatorial one would not produce the strong L-band scintillations observed in the EIA region even with a much higher ambient plasma density.

Acknowledgments
Thanks are due to K. U. Nair, Ananthi, Rupesh, P. Tiwari, and S. Banola for their technical support in the VHF scintillation experiment at Indian Institute of Geomagnetism (IIG), Department of Science and Technology, Government of India. A. B. acknowledges the Indian National Science Academy for an INSA senior scientist position and director IIG for hosting the position at IIG. S. S. acknowledges the support of the Airport Authority of India. VHF and L-band scintillation index data are available at https://doi.org/10.5281/zenodo.3355386.

References

Basu, S., McKenzie, E., & Basu, S. (1988). Ionospheric constraints on VHF/UHF communication links during solar maximum and minimum periods. *Radio Science*, *23*, 363.

Bhattacharyya, A., Groves, K. M., Basu, S., Kuenzler, H., Valladares, C. E., & Sheehan, R. (2003). L-band scintillation activity and space-time structure of low-latitude UHF scintillations. *Radio Science*, *38*, (1) 1004. https://doi.org/10.1029/2002RS002711.

Bhattacharyya, A., Kakad, B., Gurram, P., Sripathi, S., & Sunda, S. (2017). Development of intermediate-scale structure at different altitudes within an equatorial plasma bubble: Implications for L-band scintillations. *Journal of Geophysical Research: Space Physics*, *122*, 1015–1030. https://doi.org/10.1002/2016JA023478

Bhattacharyya, A., Kakad, B., Sripathi, S., Jeeva, K., & Nair, K. U. (2014). Development of intermediate scale structure near the peak of the F region within an equatorial plasma bubble. *Journal of Geophysical Research: Space Physics*, *119*, 3066–3076. https://doi.org/10.1002/2013JA019619

Bhattacharyya, A., & Yeh, K. C. (1988). Intensity correlation function for waves of different frequencies propagating through a random medium. *Radio Science*, *23*, 791–808.

Carrano, C. S., & Rino, C. L. (2016). A theory of scintillation for two-component power law irregularity spectra: Overview and numerical results. *Radio Science*, *51*, 789–813. https://doi.org/10.1002/2015RS005903

Carter, B. A., Retterer J. M., Yizengaw E., Wiens K., Wing S., Groves K., et al. (2014), Using solar wind data to predict daily GPS scintillation occurrence in the African and Asian low-latitude regions, *Geophysical Research Letters*, *41*, 8176–8184, doi:https://doi.org/10.1002/2014GL062203.

Dasgupta, A., Ray, S., Paul, A., Banerjee, P., & Bose, A. (2004). Errors in position fixing by GPS in an environment of strong equatorial scintillations in the Indian zone. *Radio Science*, *39*, RS1530. https://doi.org/10.1002/2002RS002822

de Oliveira Moraes, A., Muella, M. T. A. H., de Paula, E. R., de Oliveira, C. B. A., Terra, W. P., Perrella, W. J., & Meibach-Rosa, P. R. P. (2018). Statistical evaluation of GLONASS amplitude scintillation over low latitudes in the Brazilian territory. *Advances in Space Research*, *61*, 1776–1789.

de Paula, E. R., Muella, M. T. A. H., Sobral, J. H. A., Abdu, M. A., Batista, I. S., Beach, T. L., & Groves, K. M. (2010). Magnetic conjugate point observations of kilometer and hundred-meter scale irregularities and zonal drifts. *Journal of Geophysical Research*, *115*, A08307. https://doi.org/10.1029/2010JA015383.

Franke, S. J., & Liu, C. H. (1983). Observations and modeling of multi-frequency VHF and GHz scintillations in the equatorial region. *Journal of Geophysical Research*, *88*(A9), 7075–7085.

Franke, S. J., & Liu, C. H. (1985). Modeling of equatorial multi-frequency scintillation. *Radio Science*, *20*, 403–415.

Franke, S. J., Liu, C. H., & Fang, D. J. (1984). Multi-frequency study of ionospheric scintillation at Ascension Island. *Radio Science*, *19*, 695–706.

Groves, K. M., Basu, S., Weber, E. J., Smitham, M., Kuenzler, H., Valladares, C. E., et al. (1997). Equatorial scintillation and systems support. *Radio Science*, *32*(5), 2047–2064. https://doi.org/10.1029/97RS00836

Huba, J., & Joyce, G. (2010). Global modeling of equatorial plasma bubbles. *Geophysical Research Letters*, *37*, L17104. https://doi.org/10.1029/2010GL044281

Keskinen, M. J., Ossakow, S. L., & Fejer, B. G. (2003). Three-dimensional nonlinear evolution of equatorial ionospheric spread F bubbles. *Geophysical Research Letters*, *30*, (16) 1855. https://doi.org/10.1029/2005GL017418

Kintner, P. M., Kil, H., Beach, T. L., & de Paula, E. R. (2001). Fading time scales associated with GPS signals and potential consequences. *Radio Science*, *36*(4), 731–743.

Moraes, A. O., Rodriguez, F. S., Porella, W. J., & de Paula, E. R. (2011). Analysis of the characteristics of low-latitude GPS amplitude scintillation measured during solar maximum conditions and implications for receiver performance. *Surveys in Geophysics*, *33*(5), 1107–1131. https://doi.org/10.1007/s10712-011-9161-z

Muella, M. T. A. H., de Paula, E. R., Kantor, I. J., Rezende, L. F. C., & Smorigo, P. F. (2009). Occurrence and zonal drifts of small-scale ionospheric irregularities over an equatorial station during solar maximum—Magnetic quiet and disturbed conditions. *Advances in Space Research*, *43*, 1957–1973.

Mullen, J. P., Mackenzie, E., Basu, S., & Whitney, H. (1985). UHF/GHz scintillation observed at Ascension Island from 1980 through 1982. *Radio Science*, *20*, 357–365.

Nishioka, M., Basu, S., Basu, S., Valladares, C. E., Sheehan, R. E., Roddy, P. A., & Groves, K. M. (2011). C/NOFS satellite observations of equatorial ionospheric plasma structures supported by multiple ground-based diagnostics in October 2008. *Journal of Geophysical Research*, *116*, A10323. https://doi.org/10.1029/2011JA016446.

Retterer, J. M. (2010a). Forecasting low-latitude radio scintillation with 3-D ionospheric plume models: 1. Plume model. *Journal of Geophysical Research*, *115*, A03306. https://doi.org/10.1029/2008JA013839.

Retterer, J. M. (2010b). Forecasting low-latitude radio scintillation with 3-D ionospheric plume models: 2. Scintillation calculation. *Journal of Geophysical Research*, *115*, A03307. https://doi.org/10.1029/2008JA013840.

Rino, C., Yokoyama, T., & Carrano, C. (2018). Dynamic spectral characteristics of high-resolution simulated equatorial plasma bubbles. *Progress in Earth and Planetary Science*, *5*, 83. https://doi.org/10.1186/s40645-018-0243-0

Rino, C. L. (1979). A power law phase screen model for ionospheric scintillation, 2. Strong scatter. *Radio Science*, *14*, 1147–1155.

Rino, C. L., Carrano, C. S., Groves, K. M., & Roddy, P. A. (2016). A characterization of intermediate-scale spread F structure from four years of high-resolution C/NOFS satellite data. *Radio Science*, *51*, 779–788. https://doi.org/10.1029/2015RS005841.

Rodrigues, F. S., Kelley, M. C., Roddy, P. A., Hunton, D. E., Pfaff, R. F., de La Beaujardie`re, O., & Bust, G. S. (2009). C/NOFS observations of intermediate and transitional scale-size equatorial spread F irregularities. *Geophysical Research Letters*, *36*, L00C05. https://doi.org/10.1029/2009GL038905

Sripathi, S., Bose, S., Patra, A. K., Pant, T. K., Kakad, B., & Bhattacharyya, A. (2008). Simultaneous observations of ESF irregularities over Indian region using radar and GPS. *Annales de Geophysique*, *26*, 3197–3213.

Su, S.-Y., Yeh, H. C., & Heelis, R. A. (2001). ROCSAT 1 ionospheric plasma and electrodynamics instrument observations of equatorial spread F: An early transitional scale result. *Journal of Geophysical Research*, *106*(A12), 29,153–29,159.

Whalen, J. A. (2009). The linear dependence of GHz scintillation on electron density observed in the equatorial anomaly. *Annales de Geophysique*, *27*, 1755–1761.

Yeh, K. C., & Liu, C. H. (1982). Radio wave scintillations in the ionosphere. *Proceedings of the IEEE*, *70*(4), 324–358.

Yokoyama, T. (2017). A review on the numerical simulation of equatorial plasma bubbles towards scintillation evaluation and forecasting. *Progress in Earth and Planetary Science*, *4*, 37. https://doi.org/10.1186/s40645-017-0153-6

Yokoyama, T., Shinagawa, H., & Jin, H. (2014). Nonlinear growth, bifurcation and pinching of equatorial plasma bubble simulated by three-dimensional high-resolution bubble model. *Journal of Geophysical Research: Space Physics*, *119*, 474–10,482. https://doi.org/10.1002/2014JA020708